Time-dependent experimental identification of inter-ELM microtearing modes in the tokamak edge on DIII-D

A.O. Nelson[1,4,*] , **F.M. Laggner**[2] , **A. Diallo**[2] , **D. Smith**[3], **Z.A. Xing**[1],
R. Shousha[1] and **E. Kolemen**[1,2,*]

[1] Princeton University, Princeton, NJ 08544, United States of America
[2] Princeton Plasma Physics Laboratory, Princeton, NJ 08543, United States of America
[3] University of Wisconsin—Madison, Madison, WI 53706, United States of America
[4] Columbia University, New York, NY 10027, United States of America

E-mail: andrew.oakleigh.nelson@gmail.com and ekolemen@pppl.gov

CrossMark

Abstract
In a series of discharges on the DIII-D tokamak, fast vertical plasma jogs are used to induce current perturbations in the steep gradient region of the H-mode edge. These current perturbations directly influence the edge q profile, decoupling the resonant location and instability drive of pedestal-localized microtearing modes (MTMs). By exploiting this effect, we develop and apply a new experimental technique to track the dynamical frequency evolution of MTMs in the pedestal region, providing a compelling validation of the MTM model. The frequency of potential MTMs is calculated as the Doppler-shifted electron diamagnetic frequency at rational $q = m/n$ surfaces, showing remarkable agreement with chirped frequency behavior of $n = 3$, 4 and 5 modes detected with fast magnetics. Data is collected throughout multiple ELM cycles in order to build robust statistics describing the time-dependent frequency evolution of MTMs, which can be explained by examining the recovery of pedestal gradients after an ELM event. MTMs have a dominant transport contribution in the electron thermal channel, so the presented results indicate that reduced models of pedestal transport must be electromagnetic in nature and constructed with accurate calculations of MTM stability; inclusion of this physics is essential for accurate predictions of the electron temperature pedestal profile. Supporting measurements of mode saturation, propagation direction and transport fingerprints are made to support the dynamic frequency determination, unambiguously and experimentally identifying MTMs in the pedestal region of DIII-D.

Keywords: pedestal, MTM, turbulence, inter-ELM, vertical jogs

(Some figures may appear in colour only in the online journal)

1. Introduction

The high confinement mode (H-mode) is the most common operational scenario for many magnetic confinement fusion experiments [1]. It is characterized by the formation of an edge transport barrier (ETB), which leads to steeper pressure gradients in a region near the edge of the plasma called the pedestal. The height of the pressure pedestal is strongly correlated with the overall plasma performance: steep pedestal gradients improve plasma confinement and raise core temperatures and density. As such, in order to best understand and predict the performance of tokamak regimes, it is essential that the dynamics and limits of the pedestal be well understood.

In typical operation, the pedestal collapses periodically due to explosive magnetohydrodynamic (MHD) instabilities called edge localized modes (ELMs) [2, 3]. ELMs set a maximum

limit on the normalized pressure gradient (α) and average toroidal current density ($\langle j_{tor} \rangle$) in the pedestal region, but they do not by themselves fully constrain the achievable pedestal pressure or the resulting plasma performance [4]. Instead, the recovery of the pedestal structure between ELMs is additionally influenced by so-called microinstabilities, which regulate local profile gradients by inducing additional transport across the ETB [5]. In conjunction with the global peeling-ballooning (PB) constraint, models describing sub-critical pedestal instabilities can be used to predict the pedestal height and width, demonstrating the critical role that these microinstabilities play in determining plasma performance [6, 7].

Broadly speaking, such instabilities in the pedestal region can be categorized into groups according to their location, frequency range and behavior [8]. There are many instability candidates that may play some role in limiting the pedestal gradients prior to the critical PB-unstable threshold. Among these are kinetic ballooning modes (KBMs), microtearing modes (MTMs), electron temperature gradient modes (ETGs), ion temperature gradient modes (ITGs), trapped electron modes (TEMs), resistive ballooning modes (RBMs) and drift Alfvén waves (DAWs). In particular, models based off of KBM constraints have been extensively developed and are able to reproduce observed pedestal heights and widths to within $\sim 20\%$ on many machines [6, 7]. However, ongoing gyrokinetic work has suggested that other modes, especially the MTM [9–12], may also contribute to transport mechanisms in the pedestal region, potentially having large effects on energy regulation [13–28].

Experimental verification of the dominant transport mechanisms in the H-mode pedestal has proven difficult. Recently on DIII-D, the implementation of a new Faraday-effect polarimetry measurement has allowed for the measurement of high-frequency magnetic turbulence in the pedestal region [29]. These results were shown to be consistent with high-*n* MTM fluctuations, helping to establish the experimental existence of MTMs [26, 30]. On JET, detailed comparisons with gyrokinetic simulations showed that experimentally-observed frequency bands in magnetic fluctuations were consistent with expectations from MTMs and that MTM fluctuations produce experimentally-relevant transport [25]. Additional ongoing work at DIII-D [27, 28] and elsewhere is continuing to support the notion that MTMs are present in the H-mode pedestal, perhaps alongside additional instabilities.

In this work, we provide conclusive experimental evidence that low-*n* MTMs are present in the DIII-D pedestal by comparing the dynamic frequency evolution of inter-ELM magnetic fluctuations with MTM theory. We utilize a novel experimental approach to directly probe the characteristics of microinstabilities in the DIII-D pedestal: large and quick vertical oscillations (jogs) are used to transiently induce extra toroidal current in the pedestal region. This technique is described in more detail in section 2, where we experimentally decouple the resonant location and the instability drive of potential pedestal-localized MTMs. In section 3, a particular family of modes is shown to respond strongly to the induced current effect above a particular jogging threshold: the dynamic frequency evolution of magnetic fluctuations changes suddenly from up-chirping to down-chirping. This chirped

mode is exhaustively investigated in section 4 and is identified as an MTM through dynamic experimental analysis. Concluding remarks and outlook for future work are presented in section 5.

2. Overview of vertical jogs

Fast vertical oscillations of the plasma (jogs) have long been investigated as a method to trigger ELMs in H-mode plasmas. The effect was first reported on TCV, where experiments showed a viable avenue for ELM control by imposing a vertical plasma oscillation [31]. Since then, further investigation on AUG [32], NSTX [33], KSTAR [34], JET [35] and HL-2A [36, 37] have shown that ELMs can be reliably triggered through large, fast vertical plasma displacements. Notably, the ELMs are triggered due to the perturbation of the edge current above a critical value, which destabilizes the peeling instability. In this case, the induction of toroidal current in the pedestal is a result of plasma motion through an inhomogeneous magnetic field [38]. As such, vertical plasma jogs represent a unique perturbation method providing direct influence over the edge current.

Extending this previous work, the goal of the current experiment is to use large, fast vertical jogs not to trigger ELMs, but to induce substantial additional edge current in order to investigate the characteristics of inter-ELM microturbulence in the pedestal region. This work represents the first attempts of application of fast vertical oscillations on DIII-D, as is described below.

2.1. Fast vertical oscillations on DIII-D

In a series of DIII-D discharges, vertical oscillations are preprogrammed by artificially sending saturation level commands to each of the poloidal field (PF) shaping coils. During this time, both vertical position control and plasma shape control are temporarily lost. The response of the plasma current (I_p) to these commands is complicated, including effects from additional loop voltages generated by the changing PF coils as well as current losses from ELMs and plasma response. The saturation interval is kept very short (only ~ 5 ms in the longest case), and the shape control system is brought back online before a collision with the machine vessel walls occurs. When reactivated, the shape control system brings the plasma back to the target locations, again changing the plasma current by inducing additional loop voltages. Throughout this entire cycle, the current control system attempts to keep I_p constant by modifying the voltage ramp on the central solenoid (E-coil). Due to a large spike in the E-coil ramp during the initial jog, the time-rate-of-change of the E-coil ramp switches sign (becomes negative) during the plasma recovery for the largest jogging events.

During the course of this experiment, the jogging controls were scanned in intensity until the largest, fastest achievable jogs were obtained. A variety of successful jogging events are shown in figure 1, where the *z*-position of the plasma magnetic axis is shown as a function of time. Due to the fast motion of
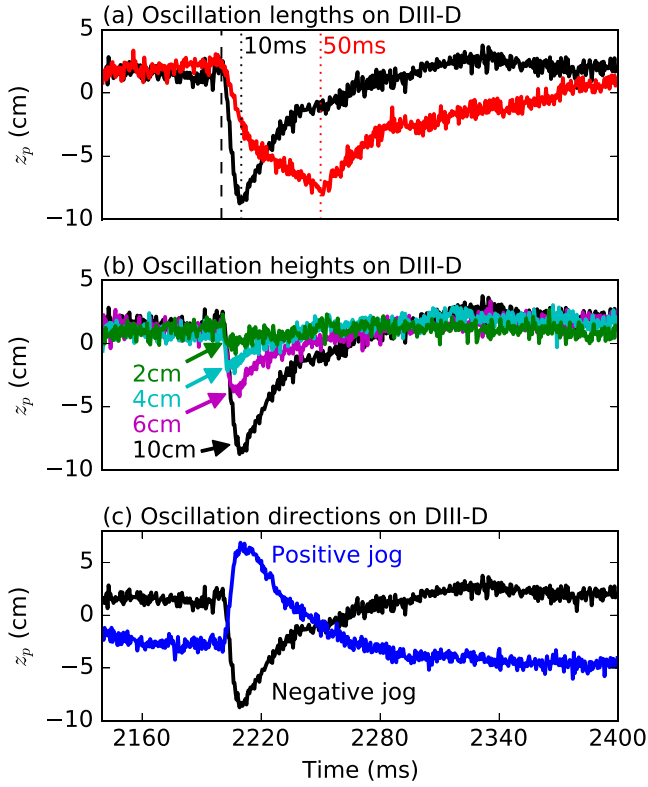
Figure 1. Varieties of vertical jogs attempted on the DIII-D tokamak. A variety of jogging (*a*) periods, (*b*) heights and (*c*) directions were executed. The largest, fastest downward jog (shown in black) is the primary kick type analyzed in this paper.

the plasma during these events (up to 10 cm in 10 ms), diagnostics measurements during and directly after the kick time were difficult. Thus, to improve the statistical uncertainty associated with plasma measurements after the jog, each jog was repeated at a frequency of 2 Hz during the discharge flattop for a total of 6 identical jogging events. The jogging behavior and plasma response were repeatable in all cases, allowing for averaging of diagnostic measurements between jogs to improve measurement statistics. The full motion of the plasma equilibrium during a jogging event is shown in figure 2.

2.2. Plasma response to vertical jogs

The plasma response to this fast vertical motion can be complicated. An equation describing the change in total toroidal edge current ($\delta I_\phi^{w_r}$) due to fast plasma motion through an inhomogeneous magnetic field was derived from the MHD equation for poloidal flux by Artola *et al* [38] and is reproduced here:

$$\delta I_\phi^{w_r} = \frac{4\pi}{\mu_0 R_0} \left[\delta\psi_{\text{ext}}(a) - B_\theta(r_0)R_0\delta w_r - \eta J_\phi \delta t \right], \quad (1)$$

where the change in current density δJ_ϕ is given by

$$\delta J_\phi = \frac{1}{2\pi r_0 w_r} \left(\delta I_\phi^{w_r} - I_\phi^{w_r} \frac{\delta w_r}{w_r} \right). \quad (2)$$

In this representation, w_r refers to the width of the edge region and r_0 to the minor radius of the inner edge of the edge region such that $w_r/r_0 \ll 1$ and the plasma edge a is given by $a(t) =$
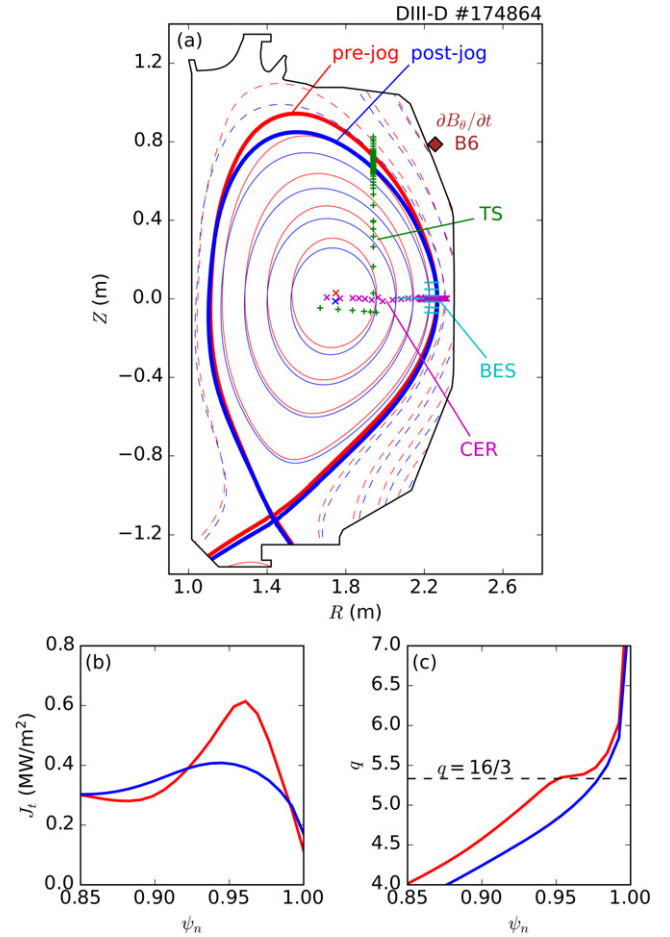

Figure 2. (*a*) Two equilibria (pre-jog: red and post-jog: blue) are shown with the locations of essential diagnostics. Open field lines are shown with dashed lines. Several diagnostics are shown, including Thomson scattering (TS), charge exchange recombination spectroscopy (CER), beam-emission spectroscopy (BES) and a fast magnetics probe (B6). (*b*) After a jog, the edge current is diminished, resulting in (*c*) an outward shift of the edge *q* profile.

$r_0 + w_r(t)$. Further, ψ_{ext} is the external (non-plasma) contribution to the poloidal magnetic flux and η is the plasma resistivity. This equation highlights the potentially conflicting effects that can influence the total toroidal edge current $I_\phi^{w_r}$. Indeed, three primary mechanisms were identified in [38] that modify the total induced current $\delta I_\phi^{w_r}$:

(a) Local changes in the external poloidal flux: $\delta\psi_{\text{ext}}(a)$.
(b) Motion of the plasma through an inhomogeneous magnetic field: $\delta\mathbf{r} \cdot \nabla\psi_{\text{ext}}$.
(c) Plasma compression or expansion: δw_r.

Note that the last term in equation (1) can be considered to be small due to the dependence on η. For more details on the above derivation, the reader is referred to the original paper [38]. Note that the edge region width can be approximated as the skin depth $w_r \sim \sqrt{\eta/(\pi\mu_0 f)s}$, where f is the oscillation frequency, in this case approximated with the fall time associated with the jogging event.

In the cases considered here, both the gradient of external flux $\nabla\psi_{\text{ext}}$ and the plasma deformation $\delta\mathbf{r}$ play important

roles. Since the external magnetic field gradient increases as the plasma moves towards the lower X-point, a net increase of external poloidal flux drives an additional current in the opposite direction of the plasma current according to $\delta I = \delta \mathbf{r} \cdot \nabla \psi_{\text{ext}} < 0$. Intuitively, the negative sign of δI can be expected by considering the plasma as approaching a current with the same sign located at the X-point. As a result of this motion, a screening current with opposite sign must be induced in the plasma, which is concentrated at the plasma edge with a skin depth $\delta_{\text{skin}} \propto \sqrt{\eta}$. However, this effect is partially counteracted by a compression of the plasma volume during the jog event. The change in the plasma cross sectional area in these cases is a result of the vertical asymmetry of the external magnetic field produced by the PF coils. Due to this asymmetry, the top of the plasma moves faster than the X-point, reducing both the effective minor radius at the edge and the plasma cross sectional area. This compression of the plasma drives an increase in the plasma current through a term $\delta I = -B_\theta(r_0)R_0\delta w_{\text{r}} > 0$. For the downwards jogs conducted here, the shape was held close to constant so the current decrease from motion though a gradient of external flux dominates over the increase from plasma compression.

The final result is shown in figure 3, where the total plasma current is diminished by $\sim 5\%$ during the largest jogs. Note that the majority of this current is lost in a narrow edge region with the peak edge current dropping by $\gtrsim 30\%$ during the most intense jogs, as is shown in figure 2(*b*). The lost current is recovered as the plasma returns to its nominal position, with I_{p} actually briefly rising above the target value during recovery from the largest and quickest vertical oscillations. While the plasma volume calculated from kinetic equilibrium reconstructions (figure 3(*c*)) recovers rather rapidly, the poloidal magnetic field B_{p} and edge safety factor q_{95} continue to evolve for ~ 100 ms after the jogging event. Importantly, while the q profile does not vary substantially during natural inter-ELM cycles, it does change after a jogging event: the q profile moves outwards (drops at the edge) during the initial vertical drop and then back inwards (rises at the edge) during the plasma recovery. This evolution is the essential perturbation for the study of inter-ELM microinstabilities and is illustrated further in figure 2(*c*), which shows the full edge q profile calculated from reconstructed plasma equilibria directly before and after a major jogging event.

2.3. Predicted effect of jogging on pedestal instabilities

As seen in figure 2(*c*), the radial location associated with a particular rational q surfaced is directly tied to the recovery of the current profile and thus changes in time. This is the unique experimental perturbation that forms the basis for the analysis presented below. Any instability located in the pedestal region that is tied to a rational q surface, such as an MTM, will experience a dynamic radial shift after the jogging event. Importantly, the magnetic signature of such modes can vary as a function of radius [25]. Thus, if MTMs are present in the jogged discharge, a change in their magnetic signatures should be identifiable as the mode moves radially though the tokamak edge region. As an example, this effect is demonstrated on a set of modeled profiles in figure 4.
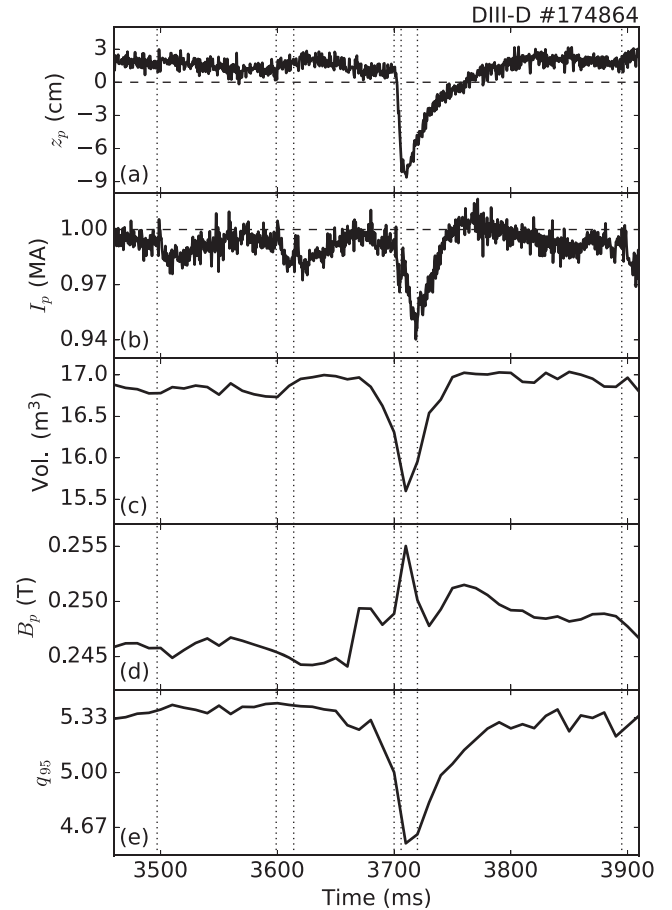

Figure 3. Plasma parameters as a function of time before and after a single jogging event. (*a*) The vertical position of the plasma. (*b*) Plasma current and (*c*) volume decrease after a jogging event, leading to a (*d*) transient increase in the poloidal magnetic field and (*e*) decrease in the edge q profile. ELM times are marked with dotted lines.

Microtearing modes are predicted to become unstable when rational q surfaces align with a peak in the electron diamagnetic frequency profile [25]. When this occurs, the modes should trigger magnetic fluctuations at a Doppler-shifted frequency defined by $\omega_{\text{MTM}}(\psi_n, t) = \omega_{\text{dop}}(\psi_n, t) + \omega_{*,\text{e}}(\psi_n, t)$. Here the electron diamagnetic frequency ($f_{\text{e}*} = \omega_{\text{e}*}/2\pi$) is given by

$$\omega_{\text{e}*} = k_y \rho_s c_s \left(\frac{1}{L_{n_e}} + \frac{1}{L_{T_e}} \right), \tag{3}$$

where $k_y = nq/a\rho_{\text{tor}}$ is the binormal wavenumber, a is the minor radius, $\rho_{\text{tor}} = \sqrt{\Phi_n}$ is the square root of the normalized toroidal magnetic flux, $\rho_s = c_s/\Omega_i$ is the sound gyroradius, $c_s = \sqrt{ZT_e}/m_i$ is the sound speed, Ω_i is the ion gyrofrequency, and the electron density and ETG scale lengths are defined as $a/L_{n_e} = (1/n_e)(dn_e/d\rho_{\text{tor}})$ and $a/L_{T_e} = (1/T_e)(dT_e/d\rho_{\text{tor}})$, respectively [9, 25]. The Doppler shift $f_{\text{dop}} = \omega_{\text{dop}}/2\pi$ is correspondingly given by:

$$\omega_{\text{dop}} = \frac{nE_{\text{r}}}{RB_{\text{p}}}, \tag{4}$$

where n is the toroidal mode number, R is the major radius, and B_{p} is the poloidal magnetic field. The radial electric field
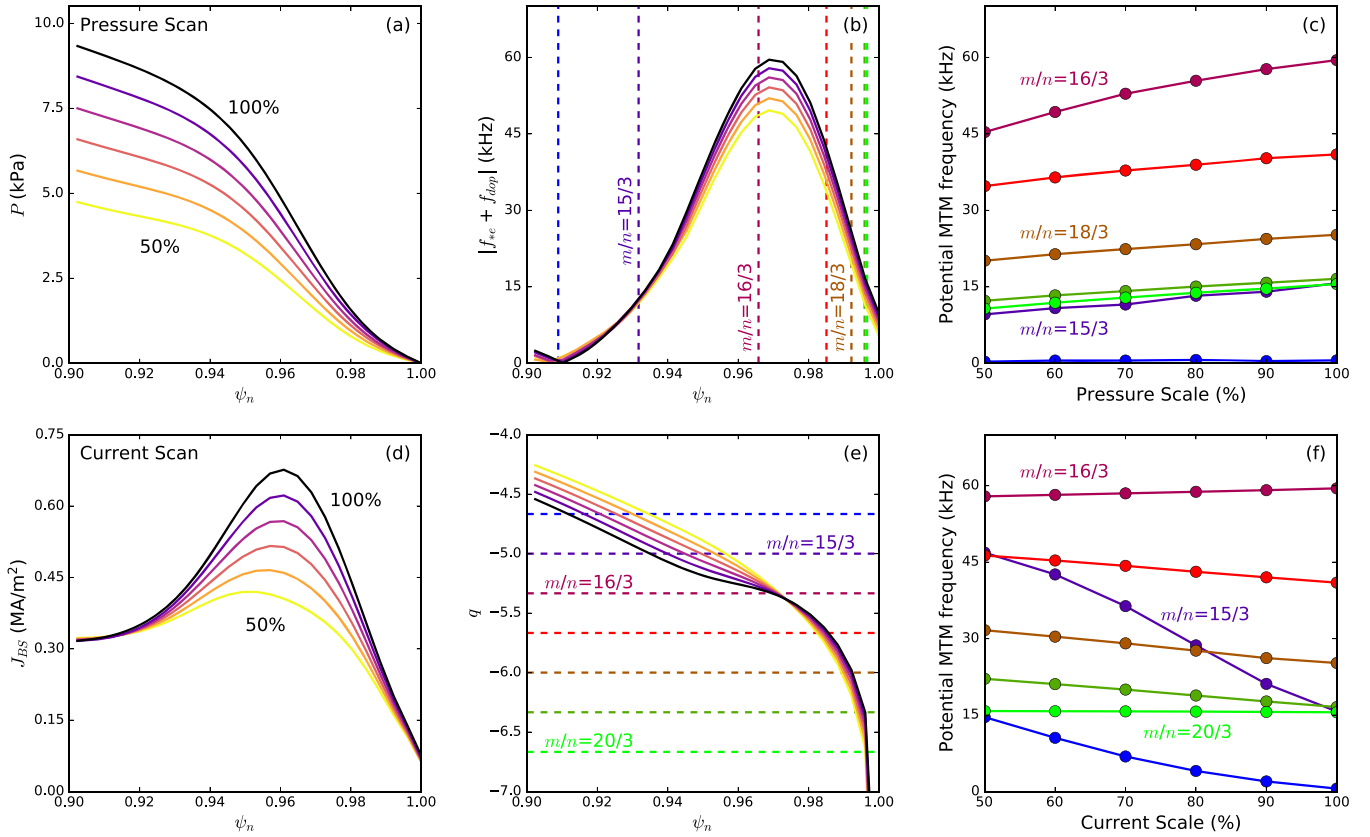
Figure 4. Demonstrative pedestal scans are completed with the VARYPED code using initial profiles from DIII-D discharge #174864.
(*a*) Increasing pressure (holding current constant) leads to (*b*) an increase in the lab frame f_{MTM} profile. (*c*) Tracking potential modes at selected rational surfaces shows a potential up-chirping behavior as the pedestal recovers. Conversely, (*d*) increasing current while holding pressure constant (*e*) changes the edge q profile. (*e*) Motion of the rational surfaces changes the MTM frequency signature, introducing downward motion to several frequency bands.

E_r is given by

$$E_{\mathrm{r}} = \frac{\nabla p}{Zen} - v_{\mathrm{p}}B_{\mathrm{t}} + v_{\mathrm{t}}B_{\mathrm{p}}, \tag{5}$$

where the biggest contribution comes from the pressure gradient term ∇p. Of course, many of the parameters in equations (3) and (4) are known to change substantially as a function of time as the pedestal recovers between ELMs. As such, the expected MTM frequency ω_{MTM} should evolve as a function of the inter-ELM recovery.

In figure 4(*a*), the typical post-ELM recovery of the H-mode pressure pedestal is modeled with VARYPED [39] by scaling the maximum pedestal pressure. In this application, VARYPED is used to modify either the pedestal pressure gradient or the edge current profile in the pedestal region, holding the rest of the pedestal parameters constant. As the temperature and density gradients change, $\omega_{*,\mathrm{e}}$ and thus ω_{MTM} will change as well, as is calculated and presented in figure 4(*b*). The Doppler shift, which will also evolve due to recovery of the E_{r} well between ELMs, is assumed to stay constant in this figure for ease of presentation. During a natural inter-ELM period, rational surfaces in the q profile remain fixed in space (examples are shown for the $n = 3$ mode in figure 4(*b*)), so the only changing component setting the potential frequency of MTM modes is the profile $\omega_{\mathrm{MTM}}(\psi_n, t)$. For each

$n = 3$ rational surface in the pedestal, regardless of whether or not it would be unstable, the potential MTM frequency is plotted in figure 4(*c*) as a function of the pedestal pressure scale, mimicking the inter-ELM evolution. While some possible MTMs demonstrate nearly constant frequency behavior, the $m/n = 16/3$ mode, which lies at the peak of the $\omega_{\mathrm{MTM}}(\psi_n)$ profile, shows a clear increasing response to the increasing pedestal pressure gradient. This signature is a direct result of the MTM assumption, so any MTM in experiment should follow the same trend.

On the other hand, this dynamic MTM signature behaves differently after a jogging event. In figure 4(*b*), a new set of VARYPED profiles is produced by scanning the maximum edge current while keeping the pressure pedestal constant. This serves as a proxy for the current recovery in the pedestal after a jogging event. Since q is a function of B_{p}, the edge q profile will evolve in concert with the edge current profile, as is shown in figure 4(*e*). Importantly, though the $\omega_{\mathrm{MTM}}(\psi_n)$ profile in this case is not a function of time (constant pressure profile), the radial location of the rational q surfaces does change in time. As such, the frequencies of potential MTMs shown in figure 4(*f*) still show a dynamical time evolution as the current evolves. Notably, some of the predicted dynamics are inverted from the predicted MTM frequency evolution after a normal ELM (figure 4(*c*)). While the $m/n = 16/3$ mode

shows a smaller frequency increase during the current evolution, the $m/n = 15/3$ MTM shows a new downward chirping frequency behavior—the MTM signature for this mode has changed.

Of course, these representative VARYPED profiles do not capture all of the complicated dynamics observed in a real experiment. Most notably, the $\omega_{\mathrm{MTM}}(\psi_n, t)$ will also evolve in time after a jogging event due to the pedestal recovery after a jog-triggered ELM. Further, E_r dynamics and plasma shape changes may change the dynamic evolution of the $\omega_{\mathrm{dop}}(\psi_n, t)$ and q profiles, respectively. Even so, this serves as a useful demonstration of the varied dynamics occurring in a post-jog inter-ELM cycle. A full model incorporating all of these effects is applied to experimental profiles in section 4.

3. Experimental observations

The discharges used in this study were lower single null H-mode discharges with plasma currents of $I_p = 1$ MA. Various levels of beam heating and electron cyclotron heating (ECH) were used throughout the scans to achieve $\beta_n \sim 1\text{–}1.7$ and $H_{98\mathrm{y}2} \sim 0.9\text{–}1.7$ with a plasma stored energy in the range of $W_{\mathrm{MHD}} \sim 0.53\text{–}0.62$ MJ. The normalized collisionality at the pedestal top for these discharges is between $\nu_{*,e} \sim 0.5\text{–}3.5$.

Despite the variation in parameters, all of these discharges display several inter-ELM modes with a distinctive mode chirping behavior between ELMs, as seen in figure 5(*b*). The toroidal mode numbers for all the observed modes below ~ 150 kHz are identified using Fourier analysis of fast-magnetic probe arrays [40] and reported in figure 5(*c*). Throughout this paper, we focus on the chirping $n = 3, 4$ and 5 modes found between 60 kHz and 140 kHz. These are colored in orange, magenta and red, respectively, in figure 5(*c*). Additional core (black) and pedestal-top (blue) modes are also present in these discharges but are not the subject of the current work. We also note that broadband magnetic fluctuations observed in these discharges by both high frequency Mirnov coils and Faraday-effect polarimetry are consistent with MTM activity in the pedestal [26, 30]. For the low-n chirped modes studied in this work, the poloidal resolution in the magnetics diagnostics is not high enough to accurately determine a poloidal mode number m, suggesting that the modes lie toward the edge of the plasma. This is confirmed in figure 6 by analysis with beam emission spectroscopy (BES) measuring density fluctuations that show both the $n = 3$ and $n = 5$ modes localized in the steep gradient region of the pedestal [41].

These observed fluctuation signatures are very similar to the 'category 1' modes described in [8], which occur in a medium frequency range ($\sim 30\text{–}150$ kHz), are localized close to the separatrix and have toroidal mode numbers in the region of $n \sim 3\text{–}8$. This type of mode has been observed on a wide variety of discharges on many different machines and looks qualitatively similar to 'washboard' modes on JET or to 'quasi-coherent fluctuations' previously identified on DIII-D [5, 8, 25, 42–44]. The analysis conducted here is expected to apply to a wide variety of tokamak discharges, though of course specific discharges should be still considered individually in future work.
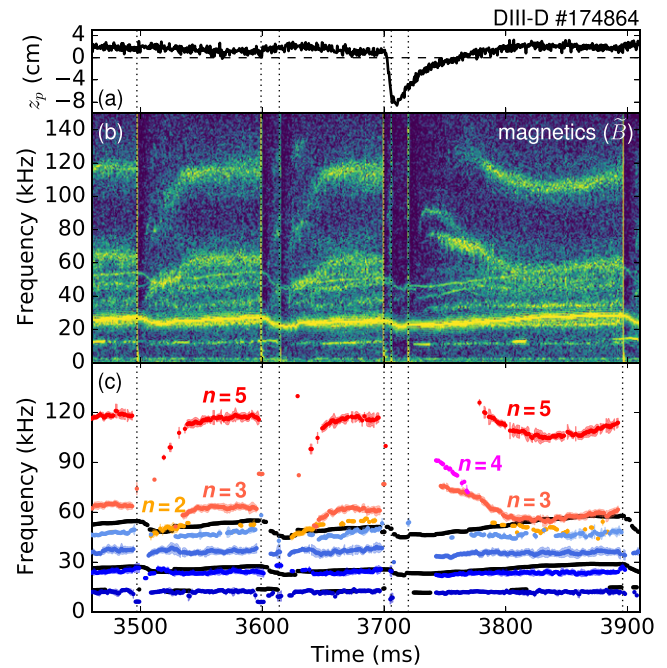

Figure 5. Over the course of two natural ELM cycles and one jog-induced ELM cycle, the (*a*) plasma vertical position and (*b*) magnetic fluctuations are plotted. (*c*) The frequencies of the orange, magenta and red $n = 3, 4$ and 5 pedestal modes display an inverted chirping behavior after the jogging event.
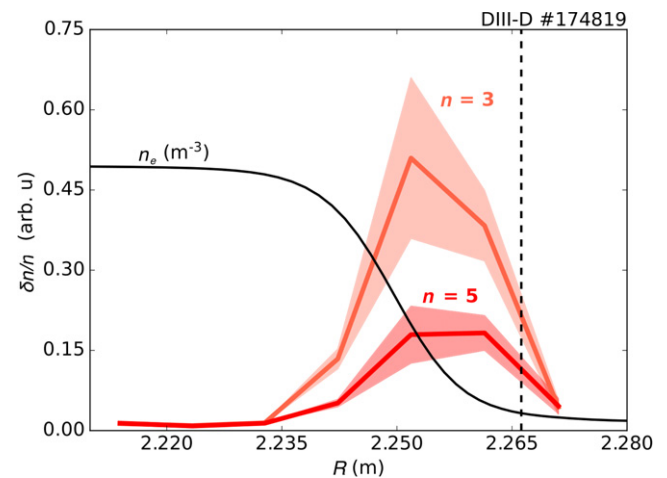

Figure 6. Mode amplitudes are localized radially with the BES diagnostic, showing that the $n = 3$ (orange) and $n = 5$ (red) modes both peak in the steep gradient region. The separatrix is shown with a vertical dashed line.

The effect of the jogging events on the edge microinstabilities can be seen in figure 5. After a natural ELM event, the observed microinstability frequency quickly rises and then saturates for the later $\sim 2/3$ of the inter-ELM period. This behavior has been previously observed and reported but not yet full explained in the literature. Notably, the behavior is distinctly different in the last inter-ELM phase shown in figure 5, which occurs directly after a large jogging event. In the post-jog recovery, the $n = 3, 4$ and 5 modes turn on at a much elevated frequency before chirping downwards to recover the same
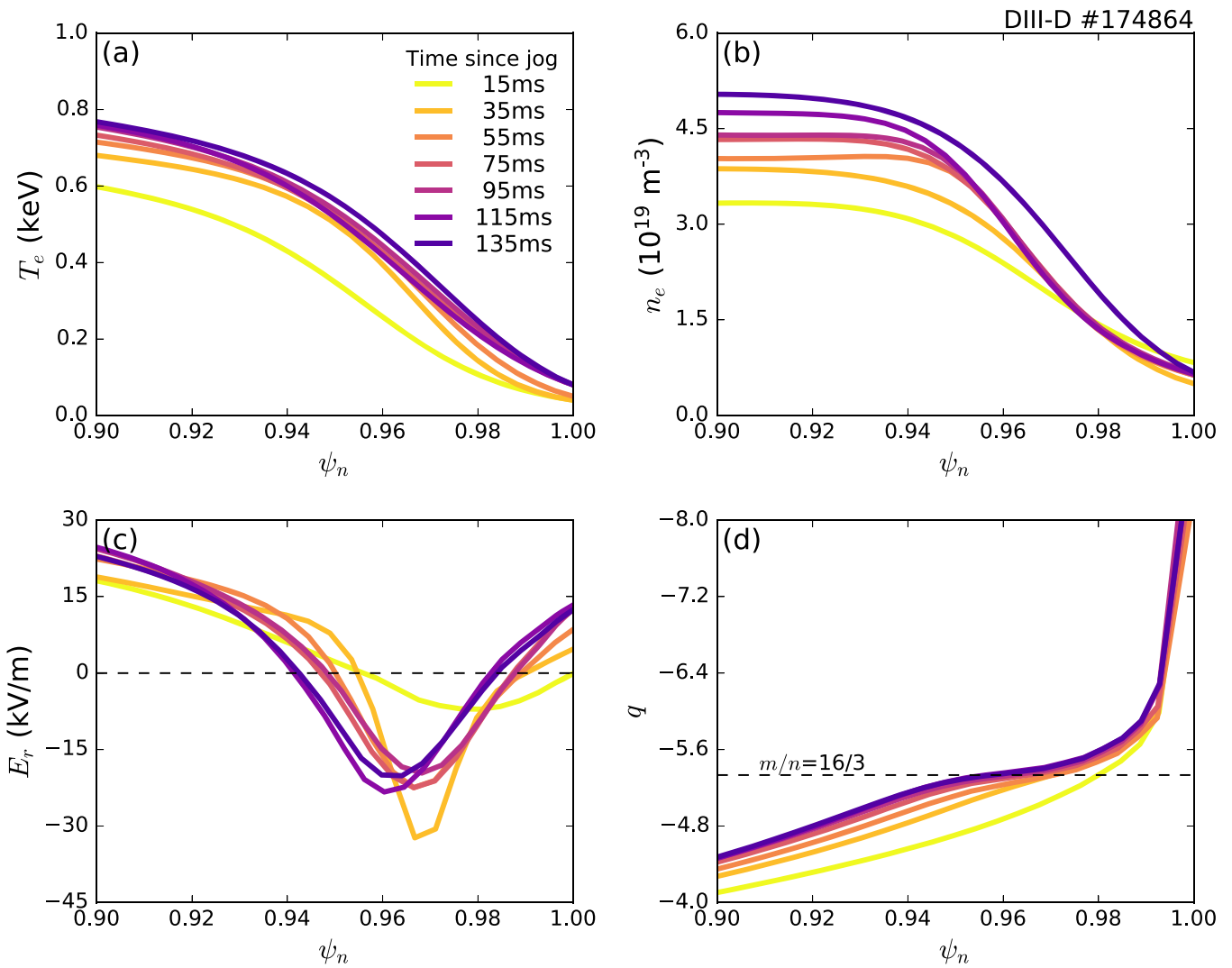
Figure 7. (*a*) T_e, (*b*) n_e, (*c*) E_r and (*d*) q profiles are shown as a function of time after a jogging event.

quasi-stationary values observed after natural ELM events. This binary switch in the jogging behavior was only observed in inter-ELM periods following the largest (6–10 cm) and fastest (10 ms) jogs in the study, suggesting that a large current perturbation is needed to induce the effect. After careful profile and equilibrium analysis, this effect can be attributed to the motion of the q profile through the edge plasma as described by MTM theory [25], providing solid experimental evidence for the existence of MTMs in the DIII-D pedestal. This analysis is discussed in detail in section 4.4.

3.1. Profile fitting

Throughout this study, OMFITprofiles [45] is used in concert with kinetic equilibrium reconstructions to produce high-fidelity pedestal profiles. Electron temperature and density profiles were reconstructed from high-resolution Thomson scattering data at the DIII-D edge [46] and fit with a modified hyperbolic tangent (`mtanh`) curves [47]. The CAKE code [48] was used to produce kinetic equilibria every 20 ms throughout the data set, in sync with the data acquisition times for ion temperature and density measurements from

charge-exchange recombination (CER) [49]. For the discharge in figure 5, kinetic equilibria were also generated manually within the OMFIT framework [50] and the PyD3D code suite [51], showing good agreement with the automatic equilibria after normal ELMing events. Due to the fast plasma motion after a jogging event, good attention was given to the equilibria, edge current profiles (with bootstrap and all Ohmic effects included) and thus q profile reconstructions throughout this study. While no direct edge q profile data were available for these discharges, q profiles from several different kinetic equilibrium reconstructions (from OMFIT, CAKE and PyD3D) were compared after jogging events to reduce error on the edge q profile calculation. Moreover, data from several different jogging events was averaged together to provide an effective uncertainty for the radial location of individual rational q surfaces after a jog. In general, the profiles are modified significantly after a jogging event due both to the triggering of several ELMs during the jog itself and the plasma motion. This is illustrated in figure 7, which shows the evolution of major event-averaged profiles after a jogging event.

The plasma current and edge q (q_{95}) are plotted in figure 3, showing that the post-jog recovery process lasts many 10s of

ms. Thus, in order to fully exploit this perturbative approach to observe changes in the inter-ELM behavior, DIII-D discharges with very long and stable inter-ELM periods, lasting ~ 100 ms each, were selected for study. Large jogs were repeated every 500 ms, allowing for several natural ELMs to occur between jogs. Data from repetitive ELMs and jogging events was averaged over the 3 s flattop period of these discharges. To get a sense of the statistical uncertainties associated with the profiles that have been computed from measurement data, the uncertainties in the data should be propagated throughout the entire analysis. The transformation that is applied to the raw data in order to obtain the Doppler-shifted electron diamagnetic frequency profile is nonlinear in nature. Since the objective is to propagate the mean and covariance information from the raw data through the nonlinear transformation, it is chosen to apply the so-called *unscented transform* (UT) to the transformations [52]. The UT follows the intuition that it should be easier to approximate a given distribution with a fixed set of parameters than it would be to approximate an arbitrary nonlinear function. A process which resembles a Monte-Carlo simulation is used, but instead of generating randomly perturbed data to the nonlinear system and reconstructing the covariance and mean from the output, a cleverly chosen set of data points (sigma-points) is used as inputs. An advantage of the UT with respect to Monte Carlo techniques is that it reduces the amount of calculations needed to calculate the final result.

The UT process used in this work can be summarized as follows: the UT needs mean ($\bar{x}$ and covariance data P_{xx}) as inputs for each of the variables used in equations (3) and (4), as well as the rational q surface location. These are then propagated through the entire nonlinear transformation and outputs $\bar{y}$ and P_{yy}. For each timeslice used, the measurement data serve as the mean $\bar{x}$ and the uncertainties are used to construct a diagonal covariance matrix P_{xx}. After the UT is applied, the Doppler-shifted electron diamagnetic frequency profile is given by $\bar{y}$, while the square root of entries of P_{yy} is taken (standard deviation) to describe the uncertainty in each entry of $\bar{y}$. In future work, P_{xx} could potentially be populated in a non-diagonal way for a more accurate error calculation; the diagonal input covariance matrix assumes that different data points within a profile exhibit no *co*-variance. However, the data needed for determining this covariance may require additional, dedicated experiments. Furthermore, visualization of the information embedded in the transformed uncertainty distribution beyond standard deviations on the profile plots is not trivial, and was thus omitted in this work. For a more detailed discussion of the mathematics behind the process, the interested reader is referred to [52].

4. Mode identification

Since no single experimental signature yet exists to identify microinstabilities, the approach taken in this paper considers every piece of experimental evidence available to form a cohesive picture of the instability dynamics. In general, leading candidates for pedestal microinstabilities are the KBM, the MTM, the ETG, the ITG and the TEM. Of these, only the KBM and the MTM are electromagnetic in nature, so these

remain as the potential candidates for the chirped modes due to the large magnetic signature observed in figure 5. The KBM is considered to be a kinetic analogue of the local MHD ballooning mode, and is destabilized near the MHD ballooning limit [53, 54]. On the other hand, the MTM is a particular example of a resistive MHD mode that requires a kinetic destabilization mechanism at finite resistivity [9, 10]. Various additional experimental characteristics of KBMs and MTMs are summarized in table 1.

After extensive experimental investigation, the chirping $n = 3, 4$ and 5 modes in figure 5 were found to be fully consistent with the observable MTM signatures presented in table 1 and inconsistent with the KBM signatures. Taken together, this provides strong support for the identification of these modes as MTMs. In the following sections, each piece of evidence is considered individually. As additional independent lines of evidence converge on the same mode type, the certainty of identification rises.

4.1. Mode drive

It is a well-established property of both KBMs and MTMs that the instabilities should saturate when a critical gradient is reached in the pedestal region [43]. After this critical gradient is reached, transport becomes stiff with additional gradient growth limited by increased turbulence. As stated in table 1, KBMs are driven by critical pressure gradients [56, 57] whereas MTMs are driven by critical ETGs [9, 11], providing a potential avenue for distinguishing between the two modes.

In figure 8, the amplitude of magnetic fluctuations for the $n = 5$ chirped mode is plotted as a function of the inter-ELM time alongside the ETG (∇T_e) evolution and the electron pressure gradient (∇p_e) evolution. The amplitude of the mode starts to grow at around ~ 5 ms after the ELM and continues until saturation is reached at about ~ 23 ms. The saturation of pedestal gradients between ELMs in these discharges is well-aligned temporally with the initial saturation of the chirped mode amplitude, marked with a blue dashed line in figure 8. In these discharges, the electron density gradient in the pedestal saturates very early after the last ELM, so both ∇p_e and ∇T_e saturate at around the same time. This makes it difficult to distinguish between saturation of the ∇T_e or ∇p_e drives at the onset of stiff transport.

As such, while calculation of the critical gradient associated with the saturation of these modes is consistent with both MTM and KBM signatures, it does not provide discerning evidence in favor of one or the other. We further note that, after ~ 35 ms, additional variation in the chirped mode amplitude is observed in both figures 5 and 8. This amplitude modulation can be explained through an analysis of the mode location with respect to the peak of the $\omega_{*,e}$ profile, as is discussed in more detail below.

Another test for mode drive can be developed by scanning the injected power with ECH, which couples strongly to the ETG. In a discharge without jogs (DIII-D #174833), 0.7 MW of P_{ECH} was injected near the pedestal top ($\rho \sim 0.86$) in order to perturb the ETGs in the pedestal region. As seen in figure 9, additional P_{ECH} raised the T_e pedestal top and increased the

Table 1. A list of identifiable characteristics for KBMs and MTMs.

| Property	KBM signature	MTM signature
State	Electromagnetic	Electromagnetic
Size	Long wavelength ($k_\theta \rho_s < 1/2$) [55]	Long wavelength ($k_\theta \rho_s \ll 1$) [16, 26]
Drive	Critical pressure gradient [56, 57]	Critical electron temperature gradient [9, 11]
Electron transport fingerprint	Transport in all channels [13] ($D_e/\chi_e \approx 2/3$)	Almost exclusively electron thermal transport [13] ($D_e/\chi_e \approx 1/10$)
Ion transport fingerprint	$\chi_i/\chi_e \approx 1$ [13]	$\chi_i/\chi_e \approx 1/10$ [13]
Impurity transport fingerprint	$D_Z/\chi_e \approx 2/3$ [13]	$D_Z/\chi_e \approx 1/10$ [13]
Frequency	$\sim 1/2\omega_{i*}$ [55]	ω_{e*} [25]
Propagation direction	Ion diamagnetic direction [55]	electron diamagnetic direction [25]
Collisionality	can exist at zero collisionality [56]	Requires finite collisionality, resistivity [10]
Growth rate	Growth rate depends non-monotonically on collisions [56]	Growth rate depends non-monotonically on collisions [26]
Shape	Generally ballooning mode structure [55]	Can peak anywhere (top + bottom in [25])
Other fluctuations	Strong relative density fluctuations [55, 56]	$|\delta B_r/B| \sim \rho_e/L_{Te}$ [26]; $\delta B/B/\delta n/n \gtrsim 0.1$ [26, 58]
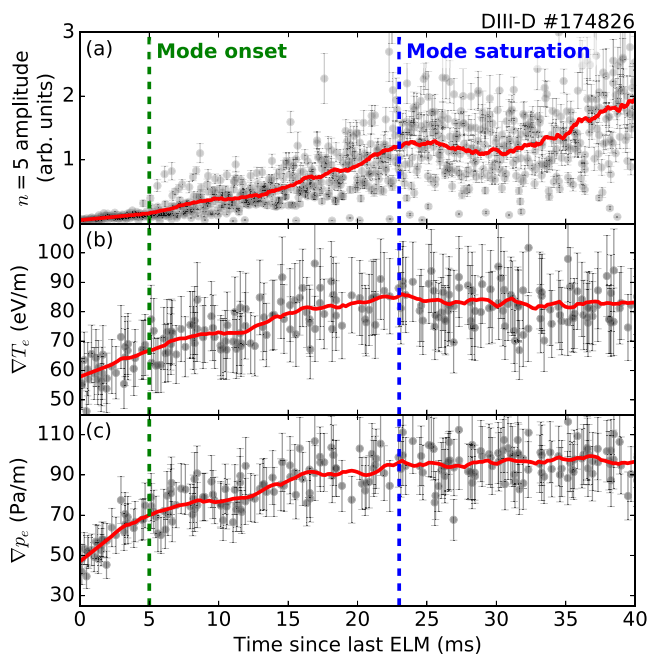
Figure 8. (*a*) The magnetic fluctuation amplitude of the $n = 5$ mode after a natural ELM is compared to (*b*) the maximum electron temperature gradient and (*c*) the maximum electron pressure gradients in the pedestal. Since the electron density gradient saturates early after an ELM ($t_{ELM} \sim 5$ ms), it is not possible to experimentally distinguish between the two gradient drives.

magnitude of the $\omega_{*,e}$ profile in the steep gradient region. The increase in ∇T_e in the pedestal region with additional electron heating is consistent with saturated MTMs contributing significantly to the electron heat flux through the pedestal region, as suggested by previous gyrokinetic studies [13]. In contrast, ∇p does not increase significantly in this discharge due to the effects of ECH density pump-out. Further, as would be expected from increased pedestal $\omega_{*,e}$, the fluctuation frequency for these modes increases with increased P_{ECH}, as shown in figures 9(*c*) and (*d*), even as the ELM frequency decreases. This behavior is again consistent with the MTM model outlined above.

4.2. Propagation direction

The propagation of the chirped modes was determined to be in the electron diamagnetic direction through two sets of agreeing analysis.

First, the maximum pedestal Doppler shift was explicitly calculated using the CER diagnostic on DIII-D. The maximum possible Doppler shift in the steep gradient region is found to be around ~ 20 kHz for the $n = 3$ mode, much less than the observed mode frequency of ~ 60 kHz. This suggests mode propagation in the electron diamagnetic direction. Further, note that the actual Doppler shift at the mode location is likely slightly less than the maximum possible Doppler shift.

Second, the propagation direction for the $n = 3, 4$ and 5 modes is determined by comparing time-lag cross correlations between vertically-separated BES channels in a 10 ms window when the mode is strongest. The Doppler shift, as calculated from CER, is also incorporated. In this BES analysis, the modes are all shown to be propagating in the upwards direction at the outboard midplane, which corresponds to the electron diamagnetic direction for clockwise toroidal fields on DIII-D.

Based on these two separate measurements, we conclude that the mode propagates in the electron diamagnetic direction in the plasma frame, consistent with MTM signatures and inconsistent with the KBM.

4.3. Transport fingerprints

Transport fingerprints for these discharges were calculated in the pedestal region as a function of time by comparing TRANSP [59, 60] and autoUEDGE [61–63] interpretive simulations. Since the modes are located in the pedestal region, which is at the edge of the regimes of applicability for both codes, a comparison between the codes was necessary to strengthen the conclusions of this study. Further, significant uncertainty exists in the determination of edge diffusivities in both TRANSP and autoUEDGE due to an inability to accurately constrain the neutral fueling profile. Neutral density measurements have recently been made possible through new diagnostic developments on DIII-D, but were not available for this study [64]. To address this limitation, neutral sensitivity
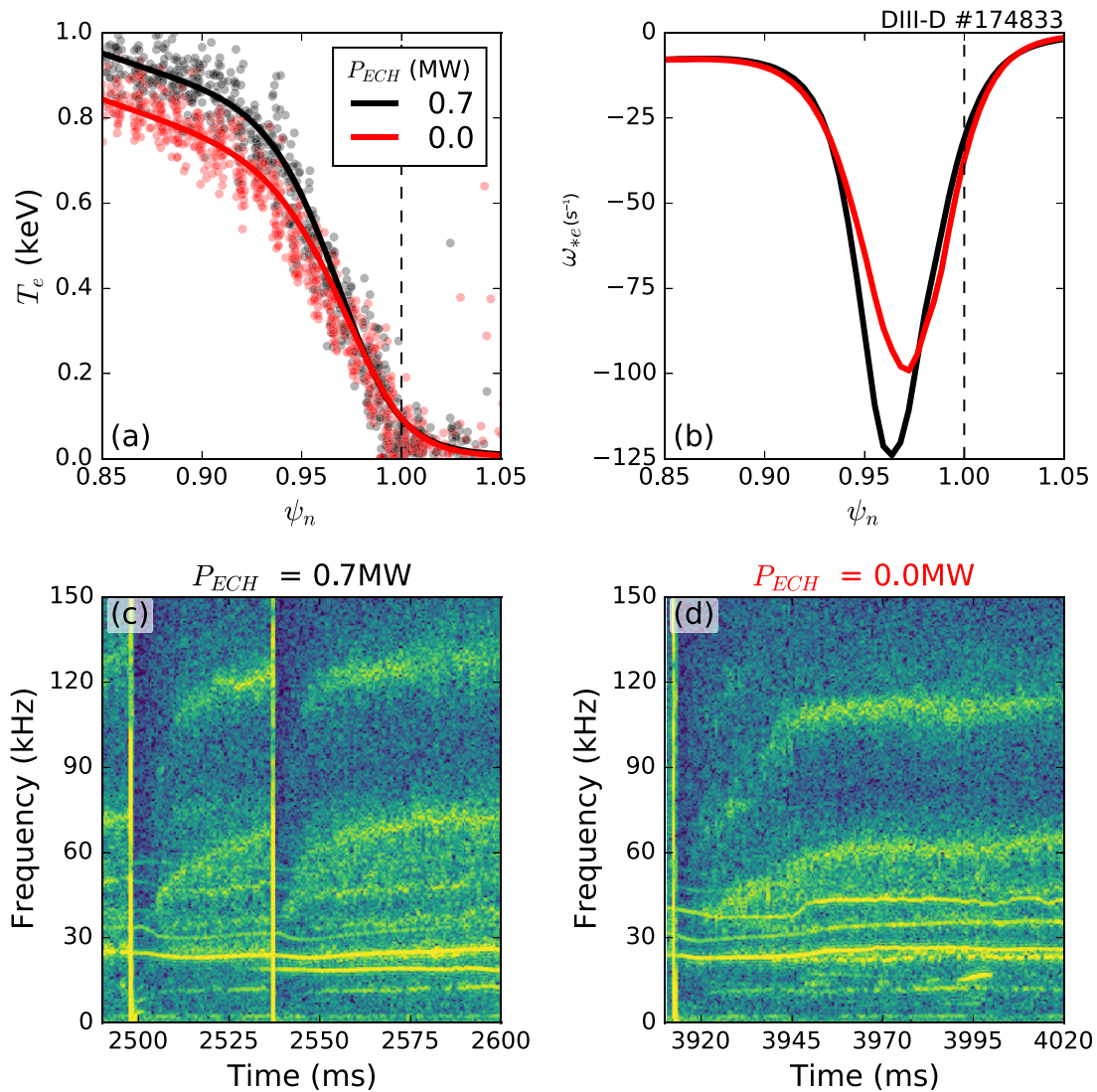
Figure 9. For a similar discharge without jogs, (*a*) the electron temperature pedestal and (*b*) the $\omega_{*,e}$ profile are found to vary with ECH injection near the plasma edge. In (*c*) and (*d*), the frequency of magnetic fluctuations associate with the chirped modes is found to increase $\sim 15\%$ with additional ECH drive.

scans were conducted in both codes by varying the particle confinement time in TRANSP and the separatrix neutral density in autoUEDGE. The results of this sensitivity scan are shown in figure 10(*a*), showing both good agreement between the two codes and relative robustness to reasonable changes in the neutral density.

The transport fingerprints for KBMs and MTMs were established by Kotschenreuther, *et al* in [13]. KBMs are MHD-like modes, which cause diffusive transport in all channels at relatively the same magnitude. While KBMs may dominate particle transport through the plasma edge, they are expected to play little role in setting the heat loss at the pedestal. In contrast, MTMs (and ETGs) are expected to contribute almost exclusively to electron thermal transport and are consistent with neoclassical χ_i with simultaneously anomalous χ_e. The fingerprint ratios for D_e/χ_e, χ_i/χ_e and D_Z/χ_e are given for both KBMs and MTMs in table 1.

The electron transport fingerprints are plotted for discharge 174819 in figure 10. In the steep gradient region, electron thermal transport dominates over both the electron diffusivity and the ion heat flow. This fingerprint is consistent with the transport fingerprint of MTMs and ETGs [13]. It should be noted, however, that this transport analysis does not apply *directly* to the chirped modes in figure 5. Instead, this global analysis suggests only that MTMs and/or ETGs play a major role in regulating the transport through the pedestal—it does not rule out the possible additional existence of KBMs or other modes acting in parallel with MTMs and/or ETGs in the pedestal. A discussion of the ion transport fingerprints is not possible for these discharges due to an inability to accurately measure the impurity ion temperature profile and thus the ion conductivity χ_i near the separatrix.

Analysis of global transport fingerprints through the pedestal region suggests that MTMs and/or ETGs likely are
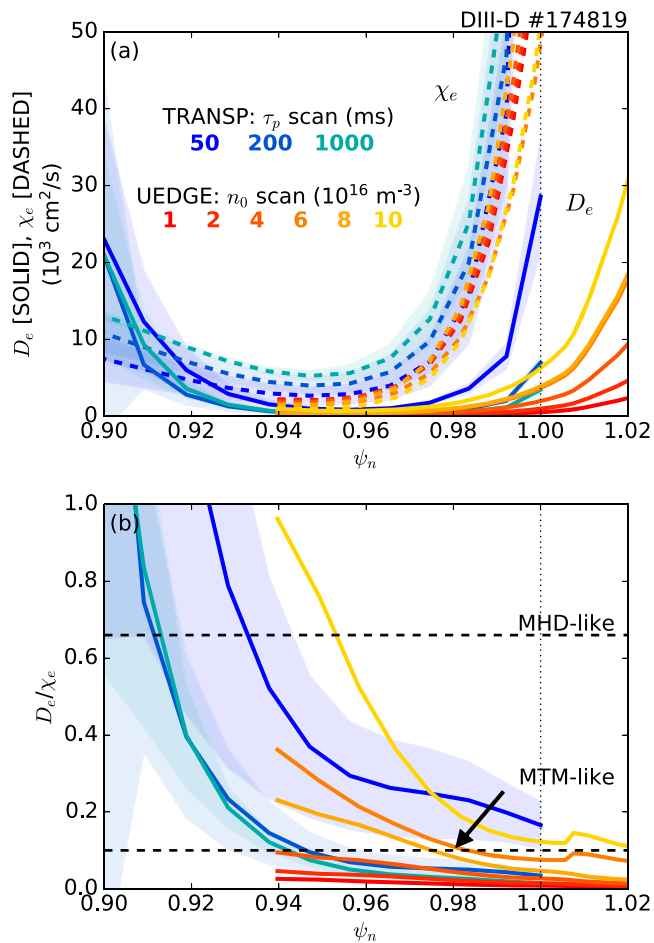
Figure 10. (*a*) Neutral density scans were conducted in autoUEDGE (red) and TRANSP (blue) to determine the transport levels across the pedestal region. (*b*) In the steep-gradient region, the observed ratio D_e/χ_e suggests that transport across the pedestal is primarily electron thermal transport, as is expected for MTMs and ETG [13].

present in this discharge and play a strong role in regulating the electron conductivity at the plasma edge.

4.4. Mode frequency

The most telling piece of evidence in this analysis is the identification of MTMs via the dynamic frequency evolution signature introduced in section 2.3. Hatch *et al* recently calculated the Doppler-shifted MTM frequency from equations (3) and (4) for quasi-stationary profiles and used this to support the observation of distinctive frequency bands observed in magnetic fluctuations [25]. In addition to the frequency bands (often referred to as 'washboard' modes), the up-chirping behavior of these modes after normal ELMs as seen in figure 5(*b*) has been observed on many machines [5, 8, 25, 42–44]. However, the time-dependence of these signatures has yet to be clearly explained. Here we use a time-dependent analysis to identify the up-chirping behavior as resulting from profile gradient recovery after an ELM event, which leads to an increase in the ω_{MTM} profile.

High resolution profile diagnostics are used to calculate ω_{e*} and ω_{dop} from equations (3) and (4), respectively, at each

available measurement time throughout entire discharges at DIII-D. These calculations are limited by the edge CER repetition rate, but since the inter-ELM period of these discharges is on the order of ~ 100 ms, averaging over several ELM cycles allows for suitably high time resolution to be achieved. The results, which show good agreement with experimental magnetic fluctuation measurements, are shown in figure 11 for natural and jogging-induced ELMs. The details of this calculation are described below.

For a representative time slice in the middle of an ELM cycle, the $n = 3\omega_{e*}$ and ω_{dop} profiles are plotted for discharge #174 864 in figure 11(*a*). Both profiles peak in the edge region due to steep gradients throughout the pedestal. It is interesting to note here that the ω_{e*} contribution dominates over the ω_{dop} contribution to the potential MTM frequency, as expected for modes propagating strongly in the electron diamagnetic direction.

Also shown in figure 11(*a*) are the rational q surfaces (vertical dashed lines) for $n = 3$ modes. Due to the absence of direct experimental measurements, accurate edge q profile reconstruction is difficult to achieve on DIII-D. Thus, to best capture the evolution of the q profile in the plasma edge, kinetic equilibrium reconstructions were made at each CER measurement time with three different methods (OMFIT, CAKE and PyD3D) as described above. After achieving agreement between the various equilibrium reconstructions, the q profiles were averaged over several ELM cycles to determine the experimental uncertainty for the q profile, which was incorporated into the proceeding calculations via an unscented transform. Through this process, the rational q surfaces in the pedestal are found to be stationary during natural inter-ELM cycles.

Comparing profile measurements across several ELM cycles allows for the time-dependent calculation of potential MTM frequencies in the pedestal region. For each possible rational q surface in the edge region, the $n = 3$ MTM frequency evolution between ELMs is presented in figure 11(*b*). In this plot, individual measurements are shown as single colored points, whereas the ELM-averaged evolution is shown with a solid line and shaded error bars. The mode with the most MTM instability drive (closest to the peak of the ω_{e*} profile: $m/n = 16/3$) shows a distinctive up-chirping behavior after a natural ELM event. When overlaid on the magnetic fluctuation measurements (figure 11(*c*)), the profile calculation shows good agreement with the $n = 3$ mode spectrogram, suggesting that this mode obeys MTM physics. This offers a simple explanation for the up-chirping behavior observed in magnetic spectrograms in references [5, 8, 25, 42–44]: as the pedestal gradients recover after an ELM, the ω_{e*} profile also rises. If an MTM is triggered during this process, its frequency will also rise until the profile gradients saturate.

Notably, the same analysis can be performed after jogging events when a significant dynamic current perturbation is present in the pedestal. As discussed above, the current perturbation modifies the edge q profile, potentially changing the MTM frequency response. This is shown for DIII-D discharge 174 864 in figure 11(*d*), which shows the evolution of both the $n = 3\omega_{MTM}$ profile and the location of the $m/n = 16/3$
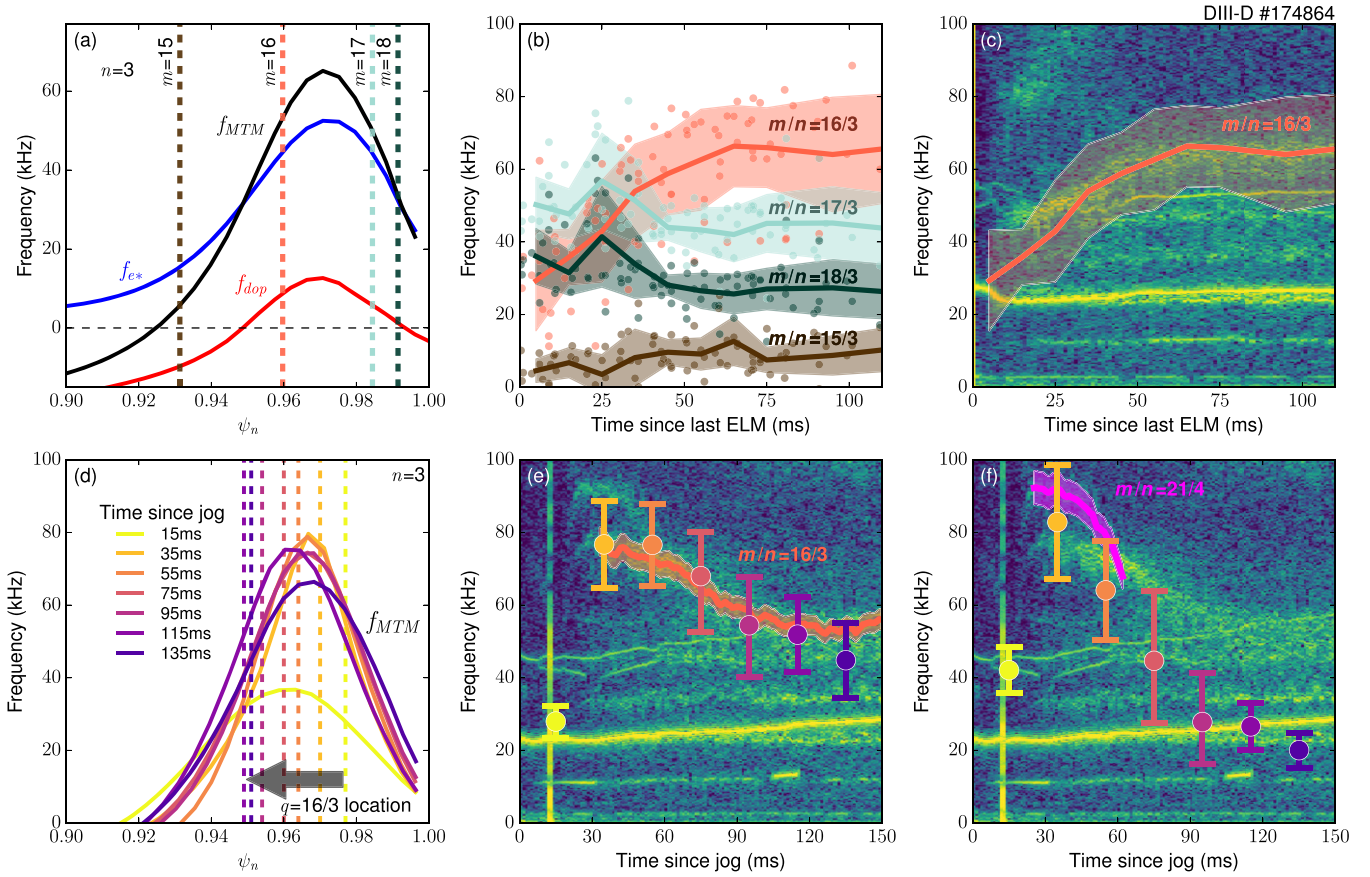
Figure 11. Equations (3) and (4) are used to dynamically predict the evolution of MTM frequency signatures after natural ELMs (*a*)−(*c*) and jogging events (*d*)−(*f*) in DIII-D discharge #174 864. (*a*) The f_{e*}, f_{dop} and f_{MTM} profiles are plotted for a representative time slice along with rational magnetic surfaces for a potential $n - 3$ mode. (*b*) For each potential rational surface, individual calculations (colored points for each *m* number) are averaged over multiple natural ELM cycles to predict the inter-ELM frequency evolution (solid line with shaded error bars) of a $n = 3$ pedestal mode. (*c*) Profile predictions for the $m/n = 16/3$ mode (same as in (*b*)) match observed $n = 3$ magnetic perturbations (spectrogram). (*d*) During the recovery after a jogging event, the $q = 16/3$ rational surface moves inwards, (*e*) creating a down-chirping behavior in the frequency prediction (colored points with UT error bars for each time slice) that matches the dynamics observed in magnetics fluctuations. (*f*) The down-chirp in the $n = 4$ fluctuation is also captured by profile-based predictions. In (*e*) and (*f*), the corresponding $n = 3$ and $n = 4$ modes are highlighted in orange and magenta, respectively, as in figure 5.

rational q surface in the plasma edge. Profiles shown here are averaged over several repetitive jogging cycles and based off of the measurements in figure 7. As expected, the relevant rational q surface moves inwards as the plasma current recovers. The effect of this radial motion is that the MTM is first triggered when the q surface aligns with the peak of the ω_{e*} profile and slowly shifts inwards down the slope of the ω_{e*} profile over ~ 100 ms. As such, the expected MTM frequency decreases after a jogging event, as shown by the colored points in figure 11(*e*). This phenomena is a result of the combination of two separate effects (the inwards evolution of the q profile and the upwards evolution of the ω_{e*} profile) acting in concert; both effects are needed to fully explain the decreasing MTM frequency in agreement with magnetic fluctuations.

In subplots 11(*e*) and (*f*), the profile-based f_{MTM} predictions (colored points with error bars) are compared directly to the highlighted chirped $n = 3$ and $n = 4$ modes identified in figure 5(*c*). Good agreement is found between the measured
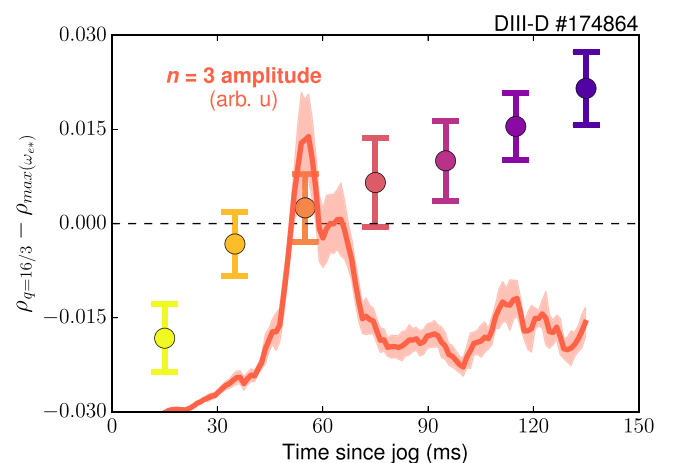

Figure 12. The evolution of the maximum amplitude of the $n = 3$ mode is compared to the separation in ρ between the $q = 16/3$ surface and the peak of the ω_{e*} profile at individual measurement times. The mode amplitude peaks when the separation is minimized.
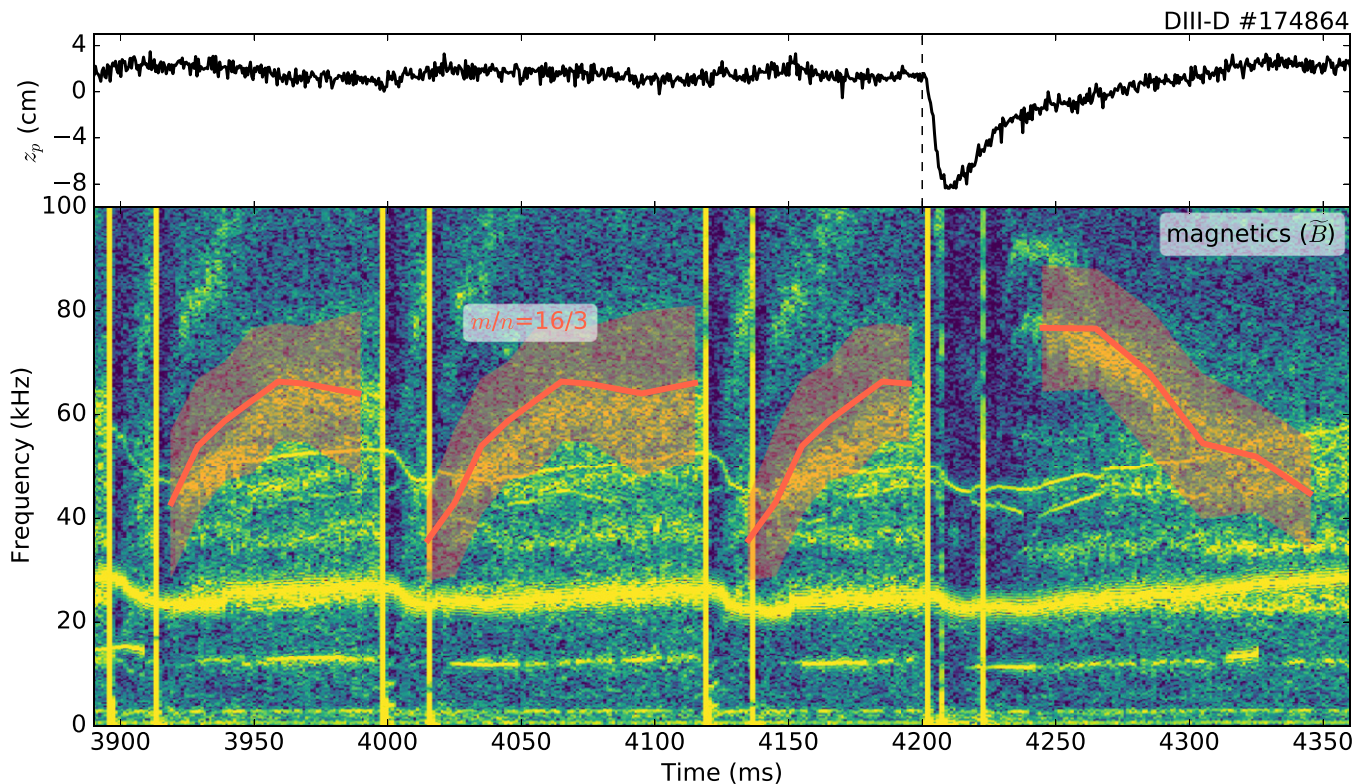
Figure 13. Profile-based predictions (orange lines with error bars) for the $m/n = 16/3$ MTM frequency are over-plotted on a magnetics spectrogram, showing good agreement with observed fluctuations (chirped modes around ~ 60 kHz) both after natural ELMs and a jogging event at ~ 4200 ms.

magnetic fluctuations and the profile-based frequency predictions. For both modes, the first calculation directly (20 ms) after a jog event occurs before the ETG is steep enough to cause the onset of MTM fluctuations. As such, the spectrograms show no labeled MTMs at the early t_{jog} times.

While the $n = 3$ frequency predictions agree with the observed fluctuations through the jogging cycle, the $n = 4$ predictions only manifest in the magnetics data between 30–60 ms after the jog. This can be simply explained by considering the radial location of the $m/n = 21/4$ mode, which lies just inside of the $m/n = 16/3$ rational surface shown in figure 11(*d*). The $q = 21/4$ surface thus starts directly on the peak of the $\omega_{\text{e}*}$ profile and quickly moves down the inward slope, falling in frequency and amplitude until it is dominated by the $n = 3$ MTM. This mode transition can be observed in figure 11(*f*) when the magenta $n = 4$ mode disappears from the magnetics spectra as the predicted $n = 4$ mode frequency dips below the $n = 3$ mode. While not explicitly shown in figure 11 to save space, we note here that the same analysis can be conducted for the chirped $n = 5$ mode as well.

Since the rational q surface moves in time after a jog while the $\omega_{\text{e}*}$ profile stays fixed in space, a further comparison can be made between the mode amplitude and the distance between the $q = 16/3$ surface and the peak of the $\omega_{\text{e}*}$ profile ($\rho_{\max(\omega_{\text{e}*})}$). This is done in figure 12, showing that the mode amplitude peaks when the rational q surface best aligns with $\rho_{\max(\omega_{\text{e}*})}$ between 50 and 70 ms after the jogging event. This again is consistent with the expectation that the electron thermal gradient, which peaks with $\omega_{*,\text{e}}$ in this discharge due to good

alignment between the temperature and density profiles, acts as the main MTM drive. The later-time evolution of the MTM amplitude is observable in this case due to the motion of the $q = 16/13$ rational surface across $\rho_{\max(\omega_{\text{e}*})}$ during the pedestal recovery. Additional variation in the mode amplitude as a function of time is likely the result of nonlinear coupling between various pedestal modes [65] and will be the subject of future work.

For the sake of clarity, the profile-based frequency calculation is plotted for the $n = 3$ mode during several consecutive ELM and jog cycles in figure 13. The profile-based predictions match all of the time-dependent behavior observed in magnetics fluctuations, both after natural ELM events and after jog-induced edge disturbances. The strength of this identification comes from good agreement with the unique mode behavior caused by intense edge current perturbations, offering a compelling validation of the MTM theory.

5. Conclusion

In this work, we use large vertical jogs to transiently induce current perturbations in the H-mode pedestal on DIII-D. These current perturbations modify the edge q profile during the recovery of pedestal gradients after an ELM, affording an opportunity to study the effect of radial motion of the q profile on microinstabilities in the pedestal region. Notably, several electromagnetic modes in the steep gradient region are shown to invert their signature inter-ELM chirping behavior.

A careful profile-based prediction of the dynamic mode frequency evolution following MTM theory is conducted, showing that the observed frequency is equal to the electron diamagnetic frequency ω_{e*} at rational $q = m/n$ surfaces. With this approach, all of the frequency dynamics observed in these discharges can be fully explained. This dynamic description, in conjunction with mode saturation with the ETG, propagation in the electron diamagnetic direction and transport fingerprints showing excessive electron thermal transport, leads to the conclusion that the chirped modes observed in this study are microtearing modes.

The presence of MTMs in the H-mode pedestal could have significant implications for pedestal physics. MTMs (in cooperation with ETGs) are expected to contribute significantly to electron thermal transport, potentially limiting the electron heat flux through the pedestal region [13]. At the present time, state-of-the-art models do not include the profile-limiting effects of MTMs into pedestal profile predictions [7], exposing a potential avenue of investigation to improve the predictive capabilities of these models. In order to predict the electron temperature profile and its evolution, reduced pedestal models must be electromagnetic in nature and should include accurate calculations of MTM stability. Of course, adding MTM stability to pedestal transport models will not be enough to fully capture the dynamics of the pedestal structure. For example, neutral fueling will also play a major role in setting the structure of the H-mode density pedestal [66, 67]. A fully comprehensive reduced model for the structure of the H-mode pedestal must include all relevant physics effects and will no doubt be the focus of extensive future work.

It is interesting here to note that, while pedestal profiles are known to vary substantially across various machines, the ratio $\nabla T_e/T_{e,\mathrm{ped}}$ has been found to be the only approximately constant pedestal scaling parameter across AUG, DIII-D and JET, though η_e is also fairly consistent [68]. Recently, this empirical constraint has been used to enable integrated modeling of core, pedestal and scrape-off-layer physics on AUG by providing a framework to define equilibrium pedestal heat flows [69]. The success of this approach implies that pedestal ∇T_e may play an important role in establishing full-device behavior. Since MTMs, which contribute primarily to electron heat flux, exist in the pedestal region, it may be possible to derive a constraint on $\nabla T_e/T_{e,\mathrm{ped}}$ directly from first principles rather than from an empirical fit. Such an approach could be extremely valuable for predict-first modeling of the edge region of future devices by providing a physics basis to expand existing pedestal models.

Finally, we note that the success of the perturbative approach applied here also implies a possibility for the expansion of dynamic turbulence identification to other unexplained tokamak regimes. Similar instability markers have been reported on a wide variety of machines and scenarios [5, 8], but the underlying physics remains largely undetermined. The experimental current perturbations described in this manuscript offer a new mechanism to uncover explanations for these observations, potentially enabling a comprehensive perturbative study of experimental transport signatures in tokamak devices.

Disclaimer

Acknowledgments

ORCID iDs

A.O. Nelson ● https://orcid.org/0000-0002-9612-1936
F.M. Laggner ● https://orcid.org/0000-0003-1601-2973
A. Diallo ● https://orcid.org/0000-0002-0706-060X
R. Shousha ● https://orcid.org/0000-0003-1498-8980
E. Kolemen ● https://orcid.org/0000-0003-4212-3247

References

[1] Wagner F. et al 1984 Development of an edge transport barrier at the H-mode transition of ASDEX Phys. Rev. Lett. **53** 1453
[2] Connor J.W., Hastie R.J., Wilson H.R. and Miller R.L. 1998 Magnetohydrodynamic stability of tokamak edge plasmas Phys. Plasmas **5** 2687
[3] Leonard A.W. 2014 Edge-localized-modes in tokamaks Phys. Plasmas **21** 090501
[4] Snyder P.B. et al 2002 Edge localized modes and the pedestal: a model based on coupled peeling-ballooning modes Phys. Plasmas **9** 2037–43
[5] Diallo A. and Laggner F.M. 2021 Review: turbulence dynamics during the pedestal evolution between edge localized modes in magnetic fusion devices Plasma Phys. Control. Fusion **63** 013001

[6] Snyder P.B., Groebner R.J., Leonard A.W., Osborne T.H. and Wilson H.R. 2009 Development and validation of a predictive model for the pedestal height *Phys. Plasmas* **16** 056118

[7] Snyder P.B., Groebner R.J., Hughes J.W., Osborne T.H., Beurskens M., Leonard A.W., Wilson H.R. and Xu X.Q. 2011 A first-principles predictive model of the pedestal height and width: development, testing and ITER optimization with the EPED model *Nucl. Fusion* **51** 103016

[8] Laggner F.M., Diallo A., Cavedon M. and Kolemen E. 2019 Inter-ELM pedestal localized fluctuations in tokamaks: summary of multi-machine observations *Nucl. Mater. Energy* **19** 479–86

[9] Hazeltine R.D., Dobrott D. and Wang T.S. 1975 Kinetic theory of tearing instability *Phys. Fluids* **18** 1778

[10] Drake J.F. and Lee Y.C. 1977 Kinetic theory of tearing instabilities *Phys. Fluids* **20** 1341

[11] Gladd N.T., Drake J.F., Chang C.L. and Liu C.S. 1980 Electron temperature gradient driven microtearing mode *Phys. Fluids* **23** 1182

[12] Drake J.F., Gladd N.T., Liu C.S. and Chang C.L. 1980 Microtearing modes and anomalous transport in tokamaks *Phys. Rev. Lett.* **44** 994

[13] Kotschenreuther M. *et al* 2019 Gyrokinetic analysis and simulation of pedestals to identify the culprits for energy losses using fingerprints *Nucl. Fusion* **59** 096001

[14] Applegate D.J., Roach C.M., Connor J.W., Cowley S.C., Dorland W., Hastie R.J. and Joiner N. 2007 Micro-tearing modes in the mega ampere spherical tokamak *Plasma Phys. Control. Fusion* **49** 1113

[15] Doerk H., Jenko F., Pueschel M.J. and Hatch D.R. 2011 Gyrokinetic microtearing turbulence *Phys. Rev. Lett.* **106** 155003

[16] Doerk H., Jenko F., Görler T., Told D., Pueschel M.J. and Hatch D.R. 2012 Gyrokinetic prediction of microtearing turbulence in standard tokamaks *Phys. Plasmas* **19** 055907

[17] Guttenfelder W. *et al* 2011 Electromagnetic transport from microtearing mode turbulence *Phys. Rev. Lett.* **106** 155004

[18] Dickinson D., Roach C.M., Saarelma S., Scannell R., Kirk A. and Wilson H.R. 2012 Kinetic instabilities that limit β in the edge of a tokamak plasma: a picture of an H-mode pedestal *Phys. Rev. Lett.* **108** 135002

[19] Dickinson D., Roach C.M., Saarelma S., Scannell R., Kirk A. and Wilson H.R. 2013 Microtearing modes at the top of the pedestal *Plasma Phys. Control. Fusion* **55** 074006

[20] Swamy A.K., Ganesh R., Chowdhury J., Brunner S., Vaclavik J. and Villard L. 2014 Global gyrokinetic stability of collisionless microtearing modes in large aspect ratio tokamaks *Phys. Plasmas* **21** 082513

[21] Swamy A.K., Ganesh R., Brunner S., Vaclavik J. and Villard L. 2015 Collisionless microtearing modes in hot tokamaks: effect of trapped electrons *Phys. Plasmas* **22** 072512

[22] Hatch D.R., Kotschenreuther M., Mahajan S., Valanju P., Jenko F., Told D., Görler T. and Saarelma S. 2016 Microtearing turbulence limiting the JET-ILW pedestal *Nucl. Fusion* **56** 104003

[23] Rafiq T., Weiland J., Kritz A.H., Luo L. and Pankin A.Y. 2016 Microtearing modes in tokamak discharges *Phys. Plasmas* **23** 6

[24] Chowdhury J., Chen Y., Wan W., Parker S.E., Guttenfelder W. and Canik J.M. 2016 Particle-in-cell δf gyrokinetic simulations of the microtearing mode *Phys. Plasmas* **23** 012513

[25] Hatch D.R. *et al* 2021 Microtearing modes as the source of magnetic fluctuations in the JET pedestal *Nucl. Fusion* **61** 036015

[26] Chen J. *et al* 2020 Internal measurement of magnetic turbulence in ELMy H-mode tokamak plasmas *Phys. Plasmas* **27** 120701

[27] Hassan E. *et al* 2021 Identifying microtearing modes in the pedestal of DIII-D H-modes in gyrokinetic simulations (private communication)

[28] Halfmoon M.R. *et al* 2021 Gyrokinetic analysis of inter-ELM transport mechanisms in DIII-D pedestals (private communication)

[29] Chen J., Ding W.X., Brower D.L., Finkenthal D. and Boivin R. 2018 A Faraday-effect polarimeter for fast magnetic dynamics measurement on DIII-D *Rev. Sci. Instrum.* **89** 10B101

[30] Chen J. *et al* 2021 Pedestal magnetic turbulence measurements in ELMy H-mode DIII-D plasmas by Faraday-effect polarimetry *Phys. Plasmas* **28** 022506

[31] Degeling A.W., Martin Y.R., Lister J.B., Villard L., Dokouka V.N., Lukash V.E. and Khayrutdinov R.R. 2003 Magnetic triggering of ELMs in TCV *Plasma Phys. Control. Fusion* **45** 1637

[32] Lang P.T. *et al* 2004 Frequency control of type-I ELMs by magnetic triggering in ASDEX Upgrade *Plasma Phys. Control. Fusion* **46** L31

[33] Gerhardt S.P. *et al* 2010 First observation of ELM pacing with vertical jogs in a spherical torus *Nucl. Fusion* **50** 064015

[34] Kim J. *et al* 2012 ELM control experiments in the KSTAR device *Nucl. Fusion* **52** 114011

[35] De La Luna E. *et al* 2016 Understanding the physics of ELM pacing via vertical kicks in JET in view of ITER *Nucl. Fusion* **56** 026001

[36] Wu N. *et al* 2017 Experiment study of edge localized mode with plasma vertical jogging in HL-2A tokamak *Phys. Plasmas* **24** 092507

[37] Wu N. *et al* 2018 Study on edge localized mode during plasma vertical swing in HL-2A tokamak *Phys. Plasmas* **25** 102505

[38] Artola F.J., Huijsmans G.T.A., Hoelzl M., Beyer P., Loarte A. and Gribov Y. 2018 Non-linear magnetohydrodynamic simulations of edge localised mode triggering via vertical position oscillations in ITER *Nucl. Fusion* **58** 096018

[39] Osborne T.H., Snyder P.B., Burrell K.H., Evans T.E., Fenstermacher M.E., Leonard A.W., Moyer R.A., Schaffer M.J. and West W.P. 2008 Edge stability of stationary ELM-suppressed regimes on DIII-D *J. Phys.: Conf. Ser.* **123** 012014

[40] Strait E.J. 2006 Magnetic diagnostic system of the DIII-D tokamak *Rev. Sci. Instrum.* **77** 023502

[41] McKee G., Ashley R., Durst R., Fonck R., Jakubowski M., Tritz K., Burrell K., Greenfield C. and Robinson J. 1999 The beam emission spectroscopy diagnostic on the DIII-D tokamak *Rev. Sci. Instrum.* **70** 913

[42] Perez C.P. *et al* 2004 Washboard modes as ELM-related events in JET *Plasma Phys. Control. Fusion* **46** 61

[43] Diallo A., Groebner R.J., Rhodes T.L., Battaglia D.J., Smith D.R., Osborne T.H., Canik J.M., Guttenfelder W. and Snyder P.B. 2015 Correlations between quasi-coherent fluctuations and the pedestal evolution during the inter-edge localized modes phase on DIII-D *Phys. Plasmas* **22** 056111

[44] Laggner F.M. *et al* 2016 High frequency magnetic fluctuations correlated with the inter-ELM pedestal evolution in ASDEX Upgrade *Plasma Phys. Control. Fusion* **58** 065005

[45] Logan N.C., Grierson B.A., Haskey S.R., Smith S.P., Meneghini O. and Eldon D. 2018 OMFIT tokamak profile data fitting and physics analysis *Fusion Sci. Technol.* **74** 125–34

[46] Eldon D. *et al* 2012 Initial results of the high resolution edge Thomson scattering upgrade at DIII-D *Rev. Sci. Instrum.* **83** 10E343

[47] Groebner R.J. *et al* 2001 Progress in quantifying the edge physics of the H mode regime in DIII-D *Nucl. Fusion* **41** 1789

[48] Xing Z.A. *et al* 2021 CAKE: consistent automatic kinetic equilibrium reconstruction *Fusion Eng. Des.* **163** 112163

[49] Chrystal C., Burrell K.H., Grierson B.A., Haskey S.R., Groebner R.J., Kaplan D.H. and Briesemeister A. 2016 Improved edge charge exchange recombination spectroscopy in DIII-D *Rev. Sci. Instrum.* **87** 11E512

[50] Meneghini O. *et al* 2015 Integrated modeling applications for tokamak experiments with OMFIT *Nucl. Fusion* **55** 083008

[51] Osborne T.H. *et al* 2015 Enhanced H-mode pedestals with lithium injection in DIII-D *Nucl. Fusion* **55** 063018

[52] Simon J., Uhlmann J. and Durrant-Whyte H.F. 2000 A new method for the nonlinear transformation of means and covariances in filters and estimators *IEEE Trans. Autom. Control* **45** 477

[53] Rewoldt G., Tang W.M. and Hastie R.J. 1987 Collisional effects on kinetic electromagnetic modes and associated quasilinear transport *Phys. Fluids* **30** 807

[54] Hong B.G., Horton W. and Choi D.I. 1989 Drift-Alfvén kinetic stability theory in the ballooning mode approximation *Phys. Fluids* B **1** 1589

[55] Yan Z., McKee G.R., Groebner R.J., Snyder P.B., Osborne T.H. and Burrell K.H. 2011 High-frequency coherent edge fluctuations in a high-pedestal-pressure quiescent H-mode plasma *Phys. Rev. Lett.* **107** 055004

[56] Wan W., Parker S.E., Chen Y., Yan Z., Groebner R.J. and Snyder P.B. 2012 Global gyrokinetic simulation of tokamak edge pedestal instabilities *Phys. Rev. Lett.* **109** 185004

[57] Snyder P.B. *et al* 2012 The EPED pedestal model and edge localized mode-suppressed regimes: studies of quiescent H-mode and development of a model for edge localized mode suppression via resonant magnetic perturbations *Phys. Plasmas* **19** 056115

[58] Hillesheim J.C., Dickinson D., Roach C.M., Saarelma S., Scannell R., Kirk A., Crocker N.A., Peebles W.A. and Meyer H. 2015 Intermediate-k density and magnetic field fluctuations during inter-ELM pedestal evolution in MAST *Plasma Phys. Control. Fusion* **58** 014020

[59] Breslau J., Gorelenkova M., Poli F., Sachdev J. and Yuan X. (2018) TRANSP. Computer Software USDOE Office of Science, Fusion Energy Sciences (SC-24)

[60] Grierson B.A. *et al* 2018 Orchestrating TRANSP simulations for interpretative and predictive tokamak modeling with OMFIT *Fusion Sci. Technol.* **74** 101–15

[61] Rognlien T.D., Milovich J.L., Rensink M.E. and Porter G.D. 1992 A fully implicit, time dependent 2D fluid code for modeling tokamak edge plasmas *J. Nucl. Mater.* **196–198** 347–51

[62] Izacard O., Kolemen E., Meneghini O., Eldon D.P. and Umansky M.V. 2018 Automatic UEDGE simulations of a large series of time-slices for tokamak discharges *60th Annual Meeting of the APS Division of Plasma Physics* (5–9 November 2018) vol 53 (https://ui.adsabs.harvard.edu/abs/2018APS.. DPPU11027I/abstract)

[63] Nelson A.O., Xing Z.A., Izacard O., Laggner F.M. and Kolemen E. 2021 Interpretative SOL modeling throughout multiple ELM cycles in DIII-D *Nucl. Mater. Energy* **26** 100883

[64] Rosenthal A.M. *et al* 2021 A 1D Lyman-alpha profile camera for plasma edge neutral studies on the DIII-D tokamak *Rev. Sci. Instrum.* **92** 033523

[65] Diallo A., Dominski J., Barada K., Knolker M., Kramer G.J. and McKee G. 2018 Direct observation of nonlinear coupling between pedestal modes leading to the onset of Edge localized modes *Phys. Rev. Lett.* **121** 235001

[66] Nelson A.O. *et al* 2020 Setting the H-mode pedestal structure: variations of particle source location using gas puff and pellet fueling *Nucl. Fusion* **60** 046003

[67] Mordijck S. 2020 Overview of density pedestal structure: role of fueling versus transport *Nucl. Fusion* **60** 082006

[68] Schneider P.A., Wolfrum E., Groebner R.J., Osborne T.H., Beurskens M.N.A., Dunne M.G., Kurzan B., Pütterich T. and Viezzer E. 2013 Analysis of temperature and density pedestal gradients in AUG, DIII-D and JET *Nucl. Fusion* **53** 073039

[69] Luda T. *et al* 2020 Integrated modeling of ASDEX Upgrade plasmas combining core, pedestal and scrape-off layer physics *Nucl. Fusion* **60** 036023